https://doi.org/10.1038/s44310-026-00110-y

Fano resonance and photoluminescence enhancement in WS_2-integrated topological insulator metasurfaces

Hua Lu[1] ✉, Dikun Li[1], Yangwu Li[1], Zengji Yue[2], Mingwen Zhang[1], Dong Mao[1], Xuetao Gan[1] & Jianlin Zhao[1] ✉

Plasmon-exciton coupling effect plays a crucial role in light emission and quantum control, which, however, has not been reported in nonmetallic systems until now. Topological insulators (TIs), with breaking through the limitations of traditional metallic materials on the operating frequency range and photonic integration, offer a new platform for exploring surface plasmons and their interaction with matter. Herein, we experimentally demonstrate the scattering resonance response of surface plasmons in the antimony telluride (Sb_2Te_3) TI metasurfaces with focused ion beam (FIB)-fabricated nanowells as well as the coupling behaviors between the plasmons and excitons in atomic-layer tungsten disulfide (WS_2) semiconductors. The measured results show that the wavelength of scattering resonance presents a redshift with increasing the depth and pitch of TI nanowells. In WS_2/TI metasurface heterostructures, we observe the obvious coupling effect between the TI plasmons and excitons in WS_2 atomic layers. The theoretical analysis reveals that the plasmon-exciton interaction is located in the weak coupling regime with the generation of Fano resonance, inducing strong photoluminescence (PL) enhancement of WS_2 atomic layers. This work will open a new door for plasmon-exciton coupling and applications of TIs in compact optoelectronic devices.

Surface plasmons are light-driven free electron oscillations at the interface between conductor and insulator with the capacities to break the light diffraction limit, confine light at the deep-subwavelength scale, and enhance near-field light intensity[1–3]. Owing to these fantastic characteristics, surface plasmons play significant roles in optical recording[3], integrated logic gates[4], ultrasensitive sensing[5], angular momentum multiplexing[6], optical nonlinearity[7], light-field control[8], all-optical modulation[9], etc. Particularly, plasmonic resonances generated in metallic nanostructures reveal ultra-small mode volume, exceptional field enhancement, and open configurations, facilitating the reinforcement of light-matter interactions[10–12]. Plasmonic resonances can find crucial applications in the improvement of nonlinear optical conversion[10], photodetection[11], and light emission[12]. Recently, plasmonic resonances have been extensively used to achieve the coupling interactions with quantum emitters[13–15]. Transition metal dichalcogenides (TMDs) with structure MX_2 (M: Mo or W, X: S or Se) are new-emerging semiconducting nanomaterials (emitters) with fascinating layer-dependent bandgap, high carrier mobility, chemical stability, and flexible integration[16–18]. Owing to the reduced Coulomb screening and 2D confinement, the atomic-layer TMDs present the strong excitonic response (excitons: electron-hole pairs) in the bandgap transition with the high transition dipole moment and large binding energy at room temperature[18–20]. TMD atomic layers offer a promising platform for plasmon-exciton coupling interactions, which enable promising applications in photoluminescence (PL) emission[14,21], plasmonic modulation[22], interface catalytic reactions[23], ultrafast optical nonlinearity[24], integrated photonic circuits[25], valley polarizations[26], etc. Until now, plasmon-exciton coupling behaviors have been extensively demonstrated in the noble metal-based plasmonic systems. Due to the intrinsic drawbacks of noble metals (e.g., poor tunability, incompatibility with standard manufacturing processes, and narrow operating frequency range), optical materials beyond noble metals have drawn special attention for exciting surface plasmons[27]. Exploring plasmon-exciton coupling in nonmetallic systems will be particularly significant for their practical applications in optoelectronic devices and integration.

Topological insulators (TIs) are a new type of quantum material with a topologically protected conducting surface (or edge) induced by the strong

[1]MOE Key Laboratory of Material Physics and Chemistry under Extraordinary Conditions, and Shaanxi Key Laboratory of Optical Information Technology, School of Physical Science and Technology, Northwestern Polytechnical University, Xi'an, China. [2]Institute of Photonic Chips, University of Shanghai for Science and Technology, Shanghai, China. ✉e-mail: hualu@nwpu.edu.cn; jlzhao@nwpu.edu.cn

spin-orbit coupling from insulating bulk[28]. The topological edge state was first reported in the 2D HgTe quantum wells with the generation of the quantum spin Hall effect[29]. Subsequently, topological surface properties were found in many 3D materials, especially Sb_2Te_3, Bi_2Te_3, Bi_2Se_3, and their compounds[30–32]. Besides excellent electronic characteristics, TIs present particularly promising optical features containing the high refractive index, giant nonlinear optical coefficient, and external tunability[33–35]. Recently, surface plasmons have been unexpectedly observed in the 3D TIs at frequencies ranging from ultraviolet (UV) to terahertz (THz)[33,36–38]. Different from conventional plasmons, TI plasmons possess the advantages of ultrabroad operating frequency range, low loss at optical frequencies, CMOS integration, etc[33,37,38]. TIs will inevitably promote the development of next-generation photonic and optoelectronic technologies[33]. Even so, plasmon-exciton coupling behaviors have not been specifically demonstrated in TI systems.

Herein, we experimentally demonstrated the scattering resonance response of surface plasmons in a type of TI metasurfaces and their coupling activities with the excitons in WS_2 atomic layers. The TI metasurfaces are composed of disk-shaped nanowells fabricated on the Sb_2Te_3 single-crystal surface by FIB lithography. The results reveal that the scattering spectrum of plasmonic resonance is dependent on the depth and pitch of TI nanowells. In the TI metasurfaces integrated with atomic-layer WS_2, we observed the distinct coupling effect between the TI plasmons and excitons in the WS_2 atomic layers. The theoretical analysis illustrates that the plasmon-exciton interactions in the WS_2/TI metasurface heterostructures are located in the weak coupling regime with the generation of Fano resonance. The weak plasmon-exciton coupling can give rise to strong PL enhancement of 15 and 25-fold for monolayer and triple-layer WS_2 on the TI metasurfaces, respectively. The results will open a new door for plasmon-exciton coupling in nonmetallic systems and applications of TIs in novel optoelectronic devices.

Results and Analysis

Fabrications and measurements of materials and TI metasurfaces

Figure 1a shows the 3D diagram of the TI metasurface integrated with a WS_2 atomic layer. Here, the Sb_2Te_3 TI was employed due to its strong topological property and good capability to support surface plasmons at optical wavelengths[30,38]. The TI metasurface consists of a disk-shaped nanowell array fabricated on a Sb_2Te_3 layer. The Sb_2Te_3 layer was mechanically exfoliated from the single-crystal bulk material and transferred onto a dielectric (Si) substrate. The Sb_2Te_3 single crystal was grown using the melting and slow-cooling method[39]. The depth, diameter, and pitch of disk-shaped nanowells are denoted by h, d, and p, respectively. The atomic-layer WS_2 was prepared by mechanically exfoliating the WS_2 single-crystal bulk material with the scotch tape, and stuck on a polydimethylsiloxane (PDMS) film. The WS_2 layer on the PDMS film was transferred onto a TI metasurface with a dry fixed-point transfer method (see Method section). As a typical TMD semiconductor, WS_2 exhibits the direct and indirect band gaps for monolayer and multilayers, respectively[16]. The WS_2 layers present the sharp absorption bands and strong excitonic resonances with the generation of intense PL in the visible region[13]. If there exists a resonant mode in TI metasurface around the WS_2 exciton wavelength, the WS_2 excitons will couple with the resonant mode, as depicted in Fig. 1b[13–15]. To verify the composition of grown TI, the energy dispersive X-ray (EDX) spectrum of a Sb_2Te_3 flake was measured using the energy dispersive spectrometer in a transmission electron microscope (TEM), as depicted in Fig. S1. The measured elemental molar ratio of Sb and Te is ~2:3, which is well consistent with the molecular formula of Sb_2Te_3. For the TEM measurement, the Sb_2Te_3 thin flakes on a Cu microgrid were prepared with the mechanical exfoliation and chemical etching methods (see Method section). Figure 1c depicts the high-angle annular dark-field (HAADF) image of a thin Sb_2Te_3 flake and the EDX mapping for Sb and Te spatial distributions. Figure 1d shows the measured selected area electron diffraction (SAED) pattern of the Sb_2Te_3 flake. The lattice spacing of 110 in the SAED pattern and the spacing of ~0.217 nm in the high-resolution TEM image clarify the high quality and hexagonal structure of the prepared Sb_2Te_3 single crystal[40]. The Sb_2Te_3 TI single crystal is an atomic-layered material that can be easily exfoliated. The layered materials enable the feasible transfer and integration with other substrates or structures. Figure 2a shows the scanning electron microscopy (SEM) image of a Sb_2Te_3 TI metasurface with disk-shaped nanowells, which was fabricated on a Sb_2Te_3 layer transferred to a silicon substrate by using FIB lithography (see Method section). An atomic force microscope (AFM) was used to measure the profile of the TI metasurface. As illustrated in Fig. 2b, the measured depth, diameter, and pitch of nanowells are $h = 100$ nm, $d = 300$ nm, and $p = 700$ nm, respectively. Figure 2c depicts the experimentally measured dark-field scattering spectrum of the TI metasurface by employing a confocal Raman spectroscopy system (see Method section). A distinct scattering resonance peak appears at the wavelength of ~587 nm. To verify the experiment result, we numerically simulated the scattering spectrum of the TI metasurface by using a finite-difference time-domain (FDTD) method (see Method section). As depicted in the inset of Fig. 2c, the simulation result is in good agreement with the experimental measurement. Another inset of Fig. 2c shows the distribution of the electric field $|E/E_i|$ 1 nm above one nanowell in the area impinged

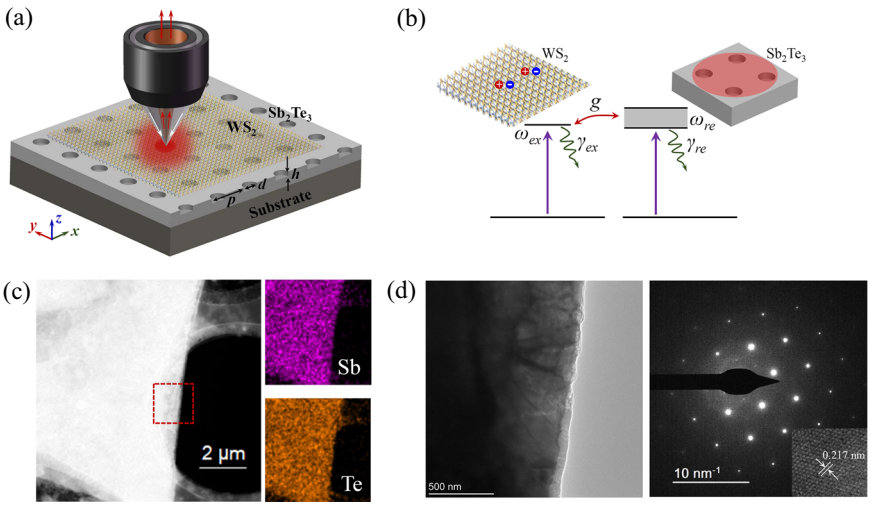

Fig. 1 | Diagram of Sb_2Te_3 TI metasurface with atomic-layer WS_2 and characterizations of Sb_2Te_3 material. a 3D diagram of the Sb_2Te_3 TI metasurface with disk-shaped nanowells covered by a WS_2 atomic layer. The height, diameter, and pitch of nanowells are h, d, and p, respectively. **b** Prototype level system for plasmon-exciton coupling process in the WS_2/TI metasurface structures. **c** TEM-measured HAADF image of a thin Sb_2Te_3 flake transferred on a Cu microgrid. The right insets are EDX mapping images of the Sb_2Te_3 flake, which determine the spatial distributions of Sb and Te elements. **d** TEM image of the Sb_2Te_3 flake in the area marked with the red dotted rectangle in (**c**). The right pictures show the SAED pattern and high-resolution TEM image (inset) of the Sb_2Te_3 flake.

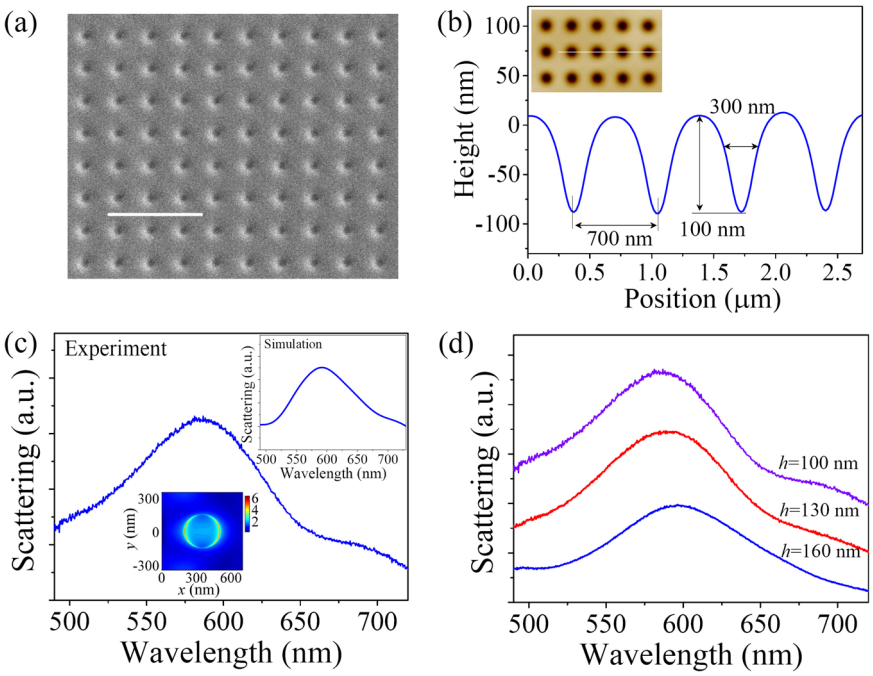

Fig. 2 | Fabrications and measurements of Sb_2Te_3 TI metasurfaces. a SEM image of a representative TI metasurface with disk-shaped nanowells fabricated on a Sb_2Te_3 flake by using the FIB lithography. The scale bar is 2 μm. **b** Measured height profile along the line in the AFM image (see the inset). **c** Measured and simulated scattering spectra of the TI metasurface with $h = 100$ nm, $d = 300$ nm, and $p = 700$ nm. The inset below shows the distribution of electric field $|E/E_i|$ 1 nm above one nanowell at the scattering peak wavelength. **d** Measured scattering spectra of the TI nanowells with different h when $d = 300$ nm and $p = 700$ nm.

with the light at the scattering peak wavelength. The electric field is obviously reinforced with the generation of plasmonic resonance in the TI nanowells. The unit size of the TI structure will determine the operating wavelength of surface plasmons. Plasmonic resonances in TI metasurfaces with hundred-nanometer wells work in the visible range, where the TMD (e.g., WS_2) exciton wavelengths are located. The existence of plasmonic resonance stems from the negative relative permittivity of Sb_2Te_3 material in the visible region[41]. Specifically, the surface state of Sb_2Te_3 TI presents negative relative permittivities similar to those of metals. At the wavelengths from 300 to 760 nm, the relative permittivity of the bulk state is also negative. Thus, both the surface and bulk states contribute to the formation of TI plasmons at the wavelengths of interest. The topological surface state enables decreasing the optical loss and improving plasmonic field enhancement. The quality factor for surface plasmons of Sb_2Te_3 TI single crystal is larger than that of gold in the 300–520 nm wavelength range, where surface plasmons of Sb_2Te_3 TI present relatively low loss. In the TI metasurfaces, the wavelengths of scattering resonance exceed this range. The scattering spectral width of Sb_2Te_3 TI nanowells becomes slightly broader than that of gold nanowells. The scattering plasmonic resonance of periodic structures relies on the unit size[42]. We fabricated the TI metasurfaces with different nanowell heights and measured the dark-field scattering spectra. As depicted in Fig. 2d, the scattering resonance peak presents a slight redshift as the nanowell height increases from 100 to 160 nm. Moreover, the scattering resonance is dependent on the pitch for plasmonic arrays[43]. Figure S2 shows the measured scattering spectrum of a TI metasurface with $h = 100$ nm, $d = 300$ nm, and $p = 750$ nm. The experiment demonstrates that a scattering resonance peak is located at a wavelength of ~623 nm, which agrees well with the simulation result. There may exist a slight fabrication error of 10% for the width of TI nanowells, which will have little effect on the peak position of the scattering resonance.

Plasmon-exciton coupling in WS_2/TI metasurface heterostructures

Subsequently, we integrated a WS_2 atomic layer with a Sb_2Te_3 TI metasurface (see Fig. S3) to study the plasmon-exciton coupling interactions. Figure 3a depicts the optical microscope image of the fabricated TI metasurface with the transferred WS_2 atomic layer. The AFM image in Fig. 3b reveals that the WS_2 layer mostly covers the TI metasurface. Figure 3c shows the AFM-measured height profiles along the lines in Fig. 3b. The depth, diameter, and pitch of the TI metasurface are $h = 135$ nm, $d = 300$ nm, and $p = 700$ nm, respectively. To verify WS_2 layer number, we measured the Raman shift spectrum of WS_2 on the TI metasurface by impinging a 532 nm CW laser, and fitted the spectrum with a multi-Lorentzian model, as can be seen in Fig. 3(d). For WS_2, the Raman modes of $A_{1g}(\Gamma)$ and $E_{2g}^1(\Gamma)$ correspond to an out-of-plane atomic vibrational mode and an in-plane vibrational mode, respectively. In Fig. 3d, the $A_{1g}(\Gamma)$ and $E_{2g}^1(\Gamma)$ modes are located at 416.7 and 354.7 cm^{-1}, whose difference is 62 cm^{-1}. This frequency difference is consistent with the reported value of monolayer WS_2[44]. Meanwhile, we measured the scattering spectrum of the WS_2/TI metasurface heterostructure, as depicted in Fig. 3e. A distinctly asymmetric spectral profile was observed around the scattering resonance peak, which resembles a Fano resonance response in optical systems[45–47]. Different from traditional Fano resonances, this Fano-like resonance in the WS_2/TI metasurface system is attributed to the coupling between the TI plasmons and WS_2 excitons[48]. The spectrally broad plasmonic resonance of TI metasurface offers a quasi-continuum state, and the spectrally narrow WS_2 exciton resonance works as a discrete state. As depicted in Fig. 1b, the coupling interference between the quasi-continuum and discrete states gives rise to the appearance of Fano resonance lineshape[49,50]. The coupling effects are common phenomena, which generally exist in atomic-layered materials/structures[51,52]. To clarify the mechanism, the coupling interaction between the TI plasmons and WS_2 excitons can also be described using the coupled oscillators model[53]. The TI plasmons and WS_2 excitons can be regarded as the two oscillators coupled with each other. In accordance with the description in Fig. 1b, ω_{ex} and ω_{re} are assumed as the resonance frequencies of WS_2 excitons and TI plasmons, respectively. γ_{ex} and γ_{re} represent the linewidths (damping rates) of excitonic and plasmonic resonances, respectively. g is the coupling strength between the two oscillators. When the harmonic wave $E(\omega)=E_0e^{-i\omega t}$ is incident onto the WS_2/TI metasurface heterostructure, the amplitudes of plasmons and

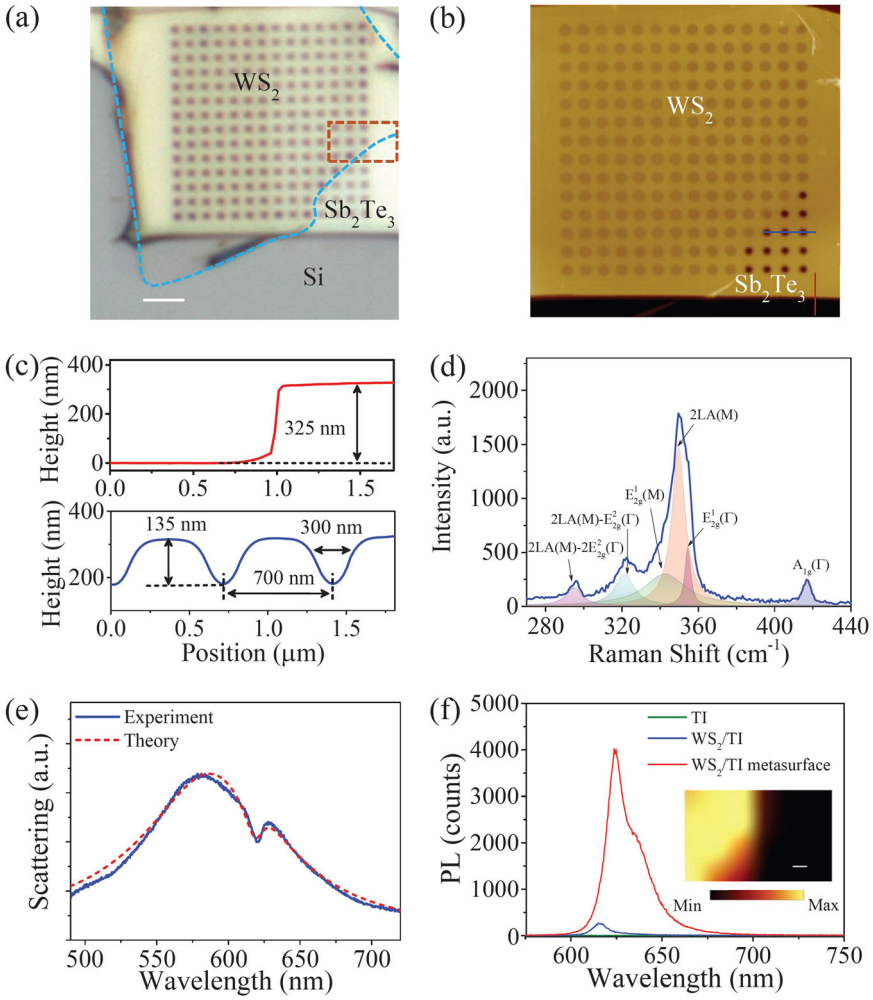

Fig. 3 | Fabricated WS_2/TI metasurface heterostructure, scattering spectra, and PL emission. **a** Optical microscope image of the TI metasurface with a transferred WS_2 atomic layer. The light-blue dashed curves mark the area of WS_2. The scale bar is 2 μm. **b** AFM image of the WS_2/TI metasurface heterostructure. **c** AFM-measured height profiles of the metasurface along the lines in (**b**). **d** Raman shift spectrum of the WS_2 atomic layer and fitted spectra with a multi-Lorentzian model. **e** Experimentally measured and theoretically fitted scattering spectra of the WS_2/TI metasurface heterostructure. **f** PL emission spectra of the Sb_2Te_3 TI, WS_2/TI, and WS_2/TI metasurface structures. The inset shows the PL intensity mapping spectrally integrated from 615 to 635 nm in the marked rectangular area of (**a**). The scale bar is 300 nm.

excitons in the coupled system can be governed by[53]

$$\begin{cases} \ddot{x}_{re} + \gamma_{re}\dot{x}_{re} + {\omega_{re}}^2 x_{re} = E_0 e^{-i\omega t} - 2g\dot{x}_{ex} \\ \ddot{x}_{ex} + \gamma_{ex}\dot{x}_{ex} + {\omega_{ex}}^2 x_{ex} = 2g\dot{x}_{re} \end{cases} \quad (1)$$

According to the coupled oscillator equations, the scattering spectrum of the coupled system could be described as[53,54]

$$\sigma_{\mathrm{scat}}(\omega) = F\omega^4 \left| \frac{\omega^2 - {\omega_{ex}}^2 + i\omega\gamma_{ex}}{(\omega^2 - {\omega_{re}}^2 + i\omega\gamma_{re})(\omega^2 - {\omega_{ex}}^2 + i\omega\gamma_{ex}) - 4\omega^2 g^2} \right|^2, \quad (2)$$

where ω is the angular frequency of incident photons, F is the scattering amplitude. By using the above equation, we can theoretically fit the measured scattering spectrum of the WS_2/TI metasurface heterostructure. As depicted in Fig. 3e, the fitted curve is in good agreement with the experimental measurement. According to the fitting results, the value of g can approach ~27.9 meV, and γ_{re} is equal to 404 meV. For monolayer WS_2, γ_{ex} is derived as ~43.8 meV, which agrees well with the reported value[55]. The large plasmonic linewidth may stem from the intrinsic absorption (loss) of Sb_2Te_3 bulk state and limited light confinement of TI nanowells at the wavelengths around 600 nm. The coupling strength g is much less than the threshold strength $g_t = (\gamma_{re}\text{-}\gamma_{ex})/4 = 90.5$ meV. According to the coupling criterion ($g<g_t$), the plasmon-exciton coupling is located in the weak-driving regime with the generation of Fano resonance. Due to the Purcell effect, the weak coupling will contribute to the PL emission enhancement of 2D semiconductors[54]. Figure 3f shows the PL emission spectra of Sb_2Te_3 TI, WS_2/TI, and WS_2/TI metasurface structures, which were measured with the confocal Raman spectroscopy with a 532 nm excitation laser. It demonstrates that the PL emission peak around the WS_2 A exciton wavelength is attributed to the WS_2 atomic layer, not the Sb_2Te_3 TI. The inset of Fig. 3f depicts the PL intensity mapping spectrally integrated from 615 to 635 nm in the marked rectangular area of Fig. 3a. Obviously, the PL intensity is stronger from the monolayer WS_2 on the TI metasurface. It shows in Fig. 3f that the PL intensity can be enhanced by a factor of 15 compared with the PL of monolayer WS_2 on the TI. Moreover, the PL peak presents a redshift of 9 nm for monolayer WS_2 on the TI metasurface. To clarify it, we employed a multi-Lorentzian model to fit the PL spectra of WS_2/TI metasurface and WS_2/TI structures[56]. The portion of A^- trions in WS_2 can distinctly increase when the laser is impinged onto the WS_2/TI metasurface heterostructure, as can be seen in Fig. S4. The wavelength of A^- trions is larger than that of A excitons, thus can give rise to the redshift of the PL peak. This may result from the electron doping (injection) of WS_2 induced by TI plasmons[56]. Generally, the structural strain of the TMD layer will also result in the redshift of PL peak with the generation of trions[57]. There may exist a strain for monolayer WS_2 integrated with the TI mesurface, which could give rise to the PL redshift. The PL peak presents a slight redshift with a narrower spectral width as the temperatue rises. The laser heating may exert little influence on the redshift and broadening of PL spectrum.

Subsequently, we fabricated another TI nanowell metasurface on a Sb_2Te_3 layer, as depicted in Fig. S5a. The AFM measurement denotes that

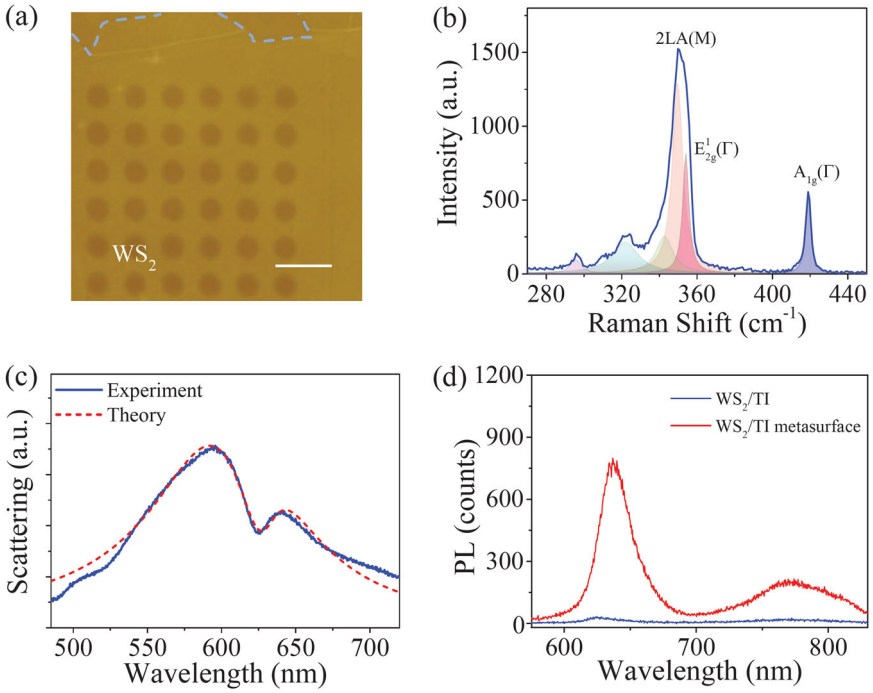

Fig. 4 | Fabricated TI metasurface with a WS_2 multilayer, scattering spectra, and PL emission. **a** AFM image of the Sb_2Te_3 TI metasurface with a WS_2 multilayer. The scale bar is 1 μm. **b** Raman shift spectrum of the WS_2 multilayer and fitted spectra with the multi-Lorentzian model. **c** Experimentally measured and theoretically fitted scattering spectra of WS_2-integrated TI metasurface with $h = 200$ nm, $d = 300$ nm, and $p = 700$ nm. **d** PL emission spectra of the WS_2 multilayer on the TI layer and metasurface structure.

the height, diameter, and pitch of TI nanowells are $h = 200$ nm, $d = 300$ nm, and $p = 700$ nm, respectively (see Figure S5b). We transferred a WS_2 multilayer on the TI metasurface to demonstrate the plasmon-exciton coupling, as shown in Fig. 4a. The result in Fig. 4b illustrates that the Raman spectrum of the transferred WS_2 multilayer possesses the obvious peaks at 354.4 and 418.9 cm^{-1} for $E_{2g}{}^1(\Gamma)$ and $A_{1g}(\Gamma)$ modes, respectively. The frequency difference between the two Raman modes is 64.5 cm^{-1}, which agrees well with the value of triple-layer (3L) WS_2[58]. As depicted in Fig. S5c, the PL emission peaks of WS_2 on the TI layer are located at the wavelengths of ~624 and 772 nm, which are attributed to the direct excitonic transition and indirect band gap emission of 3L WS_2, respectively[59]. We experimentally measured the scattering spectrum of WS_2/TI metasurface heterostructure. As depicted in Fig. 4c, the scattering spectrum also presents an asymmetric resonance line shape. A distinct dip appears at the wavelength of WS_2 A excitonic transition in the scattering spectrum of plasmonic resonance. With the coupled oscillators model, we theoretically fitted the measured scattering spectrum by employing Eq. (2). As shown in Fig. 4c, the theoretical result agrees well with the experimental measurement. The fitting results illustrate that g is ~48.9 meV, close to $\sqrt{3}$(the square root of WS_2 layer number) times as much as the coupling strength between TI plasmons and excitons in monolayer WS_2[59]. The damping rate of TI plasmons γ_{re} is ~383.1 meV. The damping rate of A excitons γ_{ex} is ~75.8 meV. The coupling strength g is less than the threshold value ($g_t = 76.8$ meV), thus the coupling effect is still located in the weak-driving regime. The asymmetric lineshape is attributed to the coupling interference between the TI plasmons and WS_2 excitons. Figure 4d depicts the PL emission spectra of 3L WS_2 on the TI layer and metasurface under the excitation of 532 nm laser. The PL intensities can be strongly enhanced for the 3L WS_2 on the TI metasurface compared to the 3L WS_2 on the TI layer. The PL intensity can be enhanced by ~25-fold. The PL emission peak around A excitons exhibits a redshift of ~12 nm for 3L WS_2 on the TI metasurface. This redshift of the PL peak for the 3L WS_2 is larger than that of monolayer WS_2 on the TI metasurface. It may stem from the stronger plasmon-induced electron doping (injection) or the strain effect of 3L WS_2 on the TI metasurface. They will give rise to the higher proportion of A^- trions in the 3L WS_2 (see Figure S5d), which results in the larger redshift of PL peak wavelength around A exciton. In this work, the strong plasmon-exciton coupling was not achieved due to the relatively large mode volume (or low quality factor) of TI plasmons in Sb_2Te_3 nanowells. The coupling strength could be further increased by optimizing the TI structures for smaller mode volume or by adding the WS_2 layer number for more excitons.

Discussion

Surface plasmons in metallic systems with strong field enhancement and open configurations offer a promising technology for light-matter interactions, especially their coupling interactions with quantum emitters. The atomically thin TMD semiconductors with excellent electronic, chemical, and optical characteristics play a crucial role in exploring plasmon-exciton coupling activities and optoelectronic applications. Plasmon-exciton coupling attracts broad attention in metallic systems with the realization of various optical functionalities. Exploring plasmon-exciton coupling interactions in nonmetallic systems is essential to enrich their applications in optoelectronic integrated devices. As new-emerging materials, TIs have presented fantastic electronic and photonic features, especially the dynamic tunability, integration, and capacity to excite surface plasmons in an ultrabroad range from UV to THz. Herein, we have demonstrated the plasmon-exciton coupling interactions in the TI system integrated with WS_2 atomic layers. By measuring the scattering spectrum, plasmonic resonance has been observed in the TI metasurfaces, which consist of disk-shaped nanowells fabricated on the Sb_2Te_3 layer by using the FIB lithography. The experiment results demonstrate that the scattering resonance wavelength presents a redshift with increasing the nanowell depth and pitch. Moreover, the WS_2 atomic layers have been innovatively integrated with the Sb_2Te_3 TI metasurfaces. The coupling behaviors between the TI plasmons and WS_2 excitons have been studied in the WS_2/TI metasurface heterostructures. Based on the coupled oscillators model, we have theoretically analyzed the coupling behaviors. It is found that the plasmon-exciton coupling is located in the weak-driving regime with a coupling strength of ~27.9 meV for monolayer WS_2. The plasmon-exciton coupling-induced Fano resonance gives rise to the strong PL enhancement of 15-fold in monolayer WS_2. The coupling strength can approach ~48.9 meV for 3L WS_2 on the TI metasurface with a PL enhancement of 25-fold. Our work will pave a new avenue for plasmon-exciton coupling interactions and applications of TIs in compact optoelectronic devices.

Methods

Growth and fabrication of Sb_2Te_3 TI

The Sb_2Te_3 TI material was grown using the melting and slow-cooling method[39]. The Sb and Te powders were mixed with an atom ratio of 2:3 in a quartz tube and heated up to 900 °C until they completely melted. Subsequently, the temperature of the melted powders dropped to 650 °C and slowly declined to 550 °C. Then, the mixed material was naturally cooled to room temperature. Thereby, the Sb_2Te_3 material can be prepared with the growth orientation along the [001] direction. The Sb_2Te_3 flakes were mechanically exfoliated from the grown Sb_2Te_3 bulk material by repeatedly tearing with scotch tape. The TI metasurfaces with disk-shaped nanowells were fabricated on the Sb_2Te_3 layer by employing the FIB lithography (FEI Helios G4 CX) with 24 pA current and 30 kV voltage. The WS_2 atomic layers were mechanically exfoliated from the WS_2 single crystal (SixCarbon Technology) with the scotch tape. The WS_2 layers were transferred onto the TI metasurface through the dry fixed-point transfer processing in a home-made optical microscope and micromanipulation system.

Material and structure characterizations

For preparing the TEM sample, the exfoliated Sb_2Te_3 TI flakes were transferred onto a SiO_2/Si substrate, and then covered by a Cu microgrid. The SiO_2/Si substrate underneath the Cu microgrid can be etched by a KOH solution droplet with ~2 mol/L concentration. After the SiO_2 layer was etched, the Sb_2Te_3 flakes can be stuck on the Cu microgrid. The EDX spectrum, HAADF image, high-resolution TEM image, and SAED of a selected Sb_2Te_3 flake were measured using the TEM instrument (FEI Talos F200X) with 200 kV voltage. The SEM images of the fabricated TI metasurface were captured employing the FIB-integrated SEM with 21 pA current and 5 kV voltage. The surface morphologies of TI metasurfaces were measured by the AFM equipment (Bruker Dimension FastScan). The dark-field scattering spectra of TI metasurfaces were measured using the confocal Raman spectroscopy (WITec Alpha 300R). The Raman shift and PL emission spectra were tested employing the confocal Raman spectroscopy with a 532 nm CW laser.

Calculation methods

The dark-field scattering spectra and field distributions of TI metasurfaces can be numerically simulated by the full-vector 3D FDTD method[60,61]. The perfectly matched layer (PML) absorbing boundary condition was set at each side of the computational space. The dark-field light source was built with two Gaussian light beams with the spot sizes of 2300 and 1900 nm as well as the different NA (e.g. NA = 0.5 and 0.495) for outer and inner lens. The phase difference between the two beams was set as π to construct an annular light source. The space area in the *x*-*y* plane was set to be larger than the Gaussian beams (e.g. 2500 nm × 2500 nm). A finite-size power monitor was properly placed above the source to detect the light backscattered from the structures, which could simulate the scattering light collected through the objective lens[60]. In the simulations, the relative permittivity of Sb_2Te_3 TI was set as the experimental data[41]. The surface and bulk states of Sb_2Te_3 TI can be simultaneously considered with a layer-on-bulk model[35,41].

Data availability

The data that support the findings of this study are available from the corresponding author upon reasonable request.

Received: 15 November 2025; Accepted: 7 February 2026;
Published online: 13 March 2026

References

1. Gramotnev, D. K. & Bozhevolnyi, S. I. Plasmonics beyond the diffraction limit. *Nat. Photonics* **4**, 83–91 (2010).
2. Fusella, M. A. et al. Plasmonic enhancement of stability and brightness in organic light-emitting devices. *Nature* **585**, 379–382 (2020).
3. Zijlstra, P., Chon, J. & Gu, M. Five-dimensional optical recording mediated by surface plasmons in gold nanorods. *Nature* **459**, 410–413 (2009).
4. Wei, H., Wang, Z., Tian, X., Käll, M. & Xu, H. Cascaded logic gates in nanophotonic plasmon networks. *Nat. Commun.* **2**, 387 (2011).
5. Caucheteur, C., Guo, T., Liu, F., Guan, B. & Albert, J. Ultrasensitive plasmonic sensing in air using optical fibre spectral combs. *Nat. Commun.* **7**, 13371 (2016).
6. Ren, H., Li, X., Zhang, Q. & Gu, M. On-chip noninterference angular momentum multiplexing of broadband light. *Science* **35**, 805–809 (2016).
7. Ren, M., Cai, W. & Xu, J. Tailorable dynamics in nonlinear optical metasurfaces. *Adv. Mater.* **32**, 1806317 (2020).
8. Li, J. et al. Simultaneous control of light polarization and phase distributions using plasmonic metasurfaces. *Adv. Funct. Mater.* **25**, 704–710 (2015).
9. Guo, X. et al. Efficient all-optical plasmonic modulators with atomically thin van der Waals heterostructures. *Adv. Mater.* **32**, 1907105 (2020).
10. Kauranen, M. & Zayats, A. V. Nonlinear plasmonics. *Nat. Photonics* **6**, 737–748 (2012).
11. Lin, K. T., Lin, H. & Jia, B. H. Plasmonic nanostructures in photodetection, energy conversion and beyond. *Nanophotonics* **9**, 3135–3163 (2020).
12. Li, G. C., Zhang, Y. L., Jiang, J., Luo, Y. & Lei, D. Y. Metal-substrate-mediated plasmon hybridization in a nanoparticle dimer for photoluminescence line-width shrinking and intensity enhancement. *ACS Nano* **11**, 3067–3080 (2017).
13. Wang, S. et al. Coherent coupling of WS_2 monolayers with metallic photonic nanostructures at room temperature. *Nano Lett.* **16**, 4368–4374 (2016).
14. Zheng, D. et al. Manipulating coherent plasmon-exciton interaction in a single silver nanorod on monolayer WSe_2. *Nano Lett.* **17**, 3809–3814 (2017).
15. Qin, J. et al. Revealing strong plasmon-exciton coupling between nanogap resonators and two-dimensional semiconductors at ambient conditions. *Phys. Rev. Lett.* **124**, 063902 (2020).
16. Zhang, X. et al. Phonon and Raman scattering of two-dimensional transition metal dichalcogenides from monolayer, multilayer to bulk material. *Chem. Soc. Rev.* **44**, 2757–2785 (2015).
17. Lin, H. et al. Engineering van der Waals materials for advanced metaphotonics. *Chem. Rev.* **122**, 15204–15355 (2022).
18. Sun, J. W. et al. Strong plasmon-exciton coupling in transition metal dichalcogenides and plasmonic nanostructures. *Nanoscale* **13**, 4408–4019 (2021).
19. Li, Y. et al. Plasmonics of 2D nanomaterials: properties and applications. *Adv. Sci.* **4**, 1600430 (2017).
20. Ghosh, S. et al. Microcavity exciton polaritons at room temperature. *Photon. Insights* **1**, R04 (2022).
21. Niu, Y., Xu, H. & Wei, H. Unified scattering and photoluminescence spectra for strong plasmon-exciton coupling. *Phys. Rev. Lett.* **128**, 167402 (2022).
22. Klein, M. et al. 2D semiconductor nonlinear plasmonic modulators. *Nat. Commun.* **10**, 3264 (2019).
23. Yang, R., Cheng, Y. Q., Song, Y. J., Belotelov, V. I. & Sun, M. T. Plasmon and plexciton driven interfacial catalytic reactions. *Chem. Rec.* **21**, 797–819 (2021).
24. Wei, K. et al. Charged biexciton polaritons sustaining strong nonlinearity in 2D semiconductor-based nanocavities. *Nat. Commun.* **14**, 5310 (2023).
25. Lee, H. S. et al. Reconfigurable exciton-plasmon interconversion for nanophotonic circuits. *Nat. Commun.* **7**, 13663 (2016).
26. Zhao, L. Y. et al. Ultrafast modulation of valley dynamics in multiple WS_2-Ag gratings strong coupling system. *PhotoniX* **3**, 5 (2022).
27. Naik, G. V., Shalaev, V. M. & Boltasseva, A. Alternative plasmonic materials: beyond gold and silver. *Adv. Mater.* **25**, 3264–3294 (2013).
28. Hasan, M. & Kane, C. Colloquium: Topological insulators. *Rev. Mod. Phys.* **82**, 3045–3067 (2010).

29. Konig, M. et al. Quantum spin hall insulator state in HgTe quantum wells. *Science* **318**, 766–770 (2007).
30. Zhang, H. et al. Topological insulators in Bi_2Se_3, Bi_2Te_3 and Sb_2Te_3 with a single Dirac cone on the surface. *Nat. Phys.* **5**, 438–442 (2009).
31. Kong, D. et al. Ambipolar field effect in the ternary topological insulator $(Bi_xSb_{1-x})_2Te_3$ by composition tuning. *Nat. Nanotechnol.* **6**, 705–709 (2011).
32. Tang, F., Po, H. C., Vishwanath, A. & Wan, X. G. Comprehensive search for topological materials using symmetry indicators. *Nature* **566**, 486 (2019).
33. Krishnamoorthy, H., Dubrovkin, A. & Adamo, G. Topological insulator metamaterials. *Chem. Rev.* **123**, 4416–4442 (2023).
34. Lu, H. et al. Strong self-enhancement of optical nonlinearity in a topological insulator with generation of Tamm state. *Laser Photon. Rev.* **17**, 2300269 (2023).
35. Lu, H. et al. λ/20-Thick cavity for mimicking electromagnetically induced transparency at telecommunication wavelengths. *Adv. Photon.* **6**, 036001 (2024).
36. Pietro, P. et al. Observation of Dirac plasmons in a topological insulator. *Nat. Nanotechnol.* **8**, 556–560 (2013).
37. Zhao, M. et al. Actively tunable visible surface plasmons in Bi_2Te_3 and their energy-harvesting applications. *Adv. Mater.* **28**, 3138–3144 (2016).
38. Yue, Z. J., Ren, H. R., Wei, S. B., Lin, J. & Gu, M. Angular-momentum nanometrology in an ultrathin plasmonic topological insulator film. *Nat. Commun.* **9**, 4413 (2018).
39. Yue, Z. J. et al. Modulation of crystal and electronic structures in topological insulators by rare-earth doping. *ACS Appl. Electron. Mater.* **1**, 1929–1936 (2019).
40. Wang, W. et al. Conversion of hexagonal Sb_2Te_3 nanoplates into nanorings driven by growth temperature. *Langmuir* **27**, 815–819 (2011).
41. Lu H., Li D., Li Y., Yue Z., Zhao J. Topological insulator plasmonics and enhanced light-matter interactions. In: Peng Y., Xu H., Wang Z., editors. Plasmon-enhanced light-matter interactions. Springer; p. 89-116. (2022)
42. Zhang, Y. N. et al. Extremely polarized and efficient hot electron intraband luminescence from aluminum nanostructures for nonlinear optical encoding. *Laser Photon. Rev.* **15**, 2000339 (2021).
43. Gopinath, A., Boriskina, S., Feng, N., Reinhard, B. & Negro, L. Photonic-plasmonic scattering resonances in deterministic aperiodic structures. *Nano Lett.* **8**, 2423–2431 (2008).
44. Peimyoo, N. et al. Thermal conductivity determination of suspended mono- and bilayer WS_2 by Raman spectroscopy. *Nano Res* **8**, 1210–1221 (2015).
45. Liu, S. D. et al. Polarization-independent multiple Fano resonances in plasmonic nonamers for multimode-matching enhanced multiband second-harmonic generation. *ACS Nano* **10**, 1442–1453 (2016).
46. Zhang, S. et al. Pronounced Fano resonance in single gold split nanodisks with 15 nm split gaps for intensive second harmonic generation. *ACS Nano* **10**, 11105–11114 (2016).
47. Fang, Z. Y. et al. Removing a wedge from a metallic nanodisk reveals a Fano resonance. *Nano Lett.* **11**, 4475–4479 (2011).
48. Wang, M. S. et al. Tunable Fano resonance and plasmon-exciton coupling in single Au nanotriangles on monolayer WS_2 at room temperature. *Adv. Mater.* **30**, 1705779 (2018).
49. Du, W. et al. Ultrafast modulation of exciton-plasmon coupling in a monolayer WS_2-Ag nanodisk hybrid system. *ACS Photonics* **6**, 2832–2840 (2019).
50. Giannini, V., Francescato, Y., Amrania, H., Phillips, C. & Maier, A. Fano resonances in nanoscale plasmonic systems: a parameter-free modeling approach. *Nano Lett.* **11**, 2835–2840 (2011).
51. Wang, Y. et al. Atomically thin noble metal dichalcogenides for phase-regulated meta-optics. *Nano Lett.* **20**, 7811–7818 (2020).
52. Pan, F. et al. Room-temperature valley-selective emission in Si-$MoSe_2$ heterostructures enabled by high-quality-factor chiroptical cavities. *Nat. Commun.* **17**, 20 (2026).
53. Wu, X. H., Gray, S. K. & Pelton, M. Quantum-dot-induced transparency in a nanoscale plasmonic resonator. *Opt. Express* **18**, 23633–23645 (2010).
54. Sun, J. W. et al. Light-emitting plexciton: exploiting plasmon-exciton interaction in the intermediate coupling regime. *ACS Nano* **12**, 10393–10402 (2018).
55. Deng, F., Liu, H. F., Xu, L., Lan, S. & Miroshnichenko, A. E. Strong exciton-plasmon coupling in a WS_2 monolayer on Au film hybrid structures mediated by liquid Ga nanoparticles. *Laser Photon. Rev.* **14**, 1900420 (2020).
56. Li, J. et al. Tuning the photo-response in monolayer MoS_2 by plasmonic nano-antenna. *Sci. Rep.* **6**, 23626 (2016).
57. Zhao, S. et al. Strain-enhanced trion emission in monolayer WS_2 modulated by an ion-gel electrochemical gate. *Appl. Phys. Lett.* **126**, 221102 (2025).
58. Chow, P. K. et al. Wetting of mono and few-layered WS_2 and MoS_2 films supported on Si/SiO_2 substrates. *ACS Nano* **9**, 3023–3031 (2015).
59. Wang, S. et al. Limits to strong coupling of excitons in multilayer WS_2 with collective plasmonic resonances. *ACS Photonics* **6**, 286–293 (2019).
60. Jiang, L. Y. et al. Accurate modeling of dark-field scattering spectra of plasmonic nano structures. *ACS Nano* **9**, 10039–10046 (2015).
61. Taflove A., Hagness S. Computational Electrodynamics: The Finite-Difference Time-Domain Method. 2nd ed. *Artech House*. (2000).

Acknowledgements

The authors thank technicians (especially Dr. Zhao C Y, Dr. Feng D, and Dr. Wang J) at the Analytical & Testing Center of Northwestern Polytechnical University for the assistance of FIB fabrication as well as AFM, SEM, EDX, and TEM measurements. This study was funded by the National Key R&D Program of China (2022YFA1404800), the National Natural Science Foundation of China (11974283, 62575241, 61705186, and 11774290), the Fundamental Research for the Central Universities (D5000240216), and Shaanxi Fundamental Science Research Project for Mathematics and Physics (23JSQ022).

Author contributions

H.L. conceived the idea, carried out the sample fabrications, characterizations, simulations, and analysis of results, as well as drew figures and wrote the manuscript text. D.L. took part in the measurements and simulations of the scattering spectra. Y.L. participated in the material characterization. Z.Y. provided the Sb_2Te_3 materials and discussed the material characterizations. M.Z. helped to transfer WS_2 onto the TI metasurface. D.M., X.G., and J.Z. discussed the methods, results, and promoted the manuscript presentation. All authors substantially contributed to the manuscript.

Competing interests

The authors declare no competing interests.

Additional information

Supplementary information The online version contains supplementary material available at https://doi.org/10.1038/s44310-026-00110-y.

Correspondence and requests for materials should be addressed to Hua Lu or Jianlin Zhao.